



## Article

# Plasmonic Sensor and Surface Enhanced Fluorescence Imaging Based on Hollow Nanocone Arrays

Pengkun Chen <sup>1</sup>, Xinyi Chen <sup>2</sup> , Mingyu Cheng <sup>2,3</sup>, Chuting Zhang <sup>1</sup>, Jin Cui <sup>1,\*</sup> and Bin Ai <sup>2,3,\*</sup> 

<sup>1</sup> United Microelectronics Center Co., Ltd., Chongqing 401332, China

<sup>2</sup> School of Microelectronics and Communication Engineering, Chongqing University, Chongqing 400044, China

<sup>3</sup> Chongqing Key Laboratory of Bio Perception & Intelligent Information Processing, Chongqing 400044, China

\* Correspondence: jin.cui@cumec.cn (J.C.); binai@cqu.edu.cn (B.A.)

**Abstract:** Hollow nanocone arrays are fabricated by a low-cost and efficient colloidal lithography (CL) technique. The hollow nanocone arrays are then reversed to make only the tips contact the substrate. The optical properties of the obverse and inverse hollow nanocone arrays are determined by the surrounding environment, showing different reflection spectra and structure dependence. The inverse hollow nanocone arrays show a relative index sensitivity of 70% per RIU with strict linearity. The fluorescence of fluorophore or staining cells can be facily enhanced by placing them on the tips of the hollow nanocone arrays, while having no quenching effect. The study of the obverse and inverse hollow nanocone arrays can benefit the understanding of the effect of the environment on the plasmonic resonances. The hollow nanocone arrays are promising to serve as high-performance plasmonic sensors and versatile substrates for surface-enhanced fluorescence imaging.

**Keywords:** plasmonic sensors; colloidal lithography; surface plasmon resonance; nanofabrication



**Citation:** Chen, P.; Chen, X.; Cheng, M.; Zhang, C.; Cui, J.; Ai, B.

Plasmonic Sensor and Surface Enhanced Fluorescence Imaging Based on Hollow Nanocone Arrays. *Chemosensors* **2022**, *10*, 431. <https://doi.org/10.3390/chemosensors10100431>

Academic Editor: Marco Pisco

Received: 17 September 2022

Accepted: 17 October 2022

Published: 18 October 2022

**Publisher's Note:** MDPI stays neutral with regard to jurisdictional claims in published maps and institutional affiliations.



**Copyright:** © 2022 by the authors. Licensee MDPI, Basel, Switzerland. This article is an open access article distributed under the terms and conditions of the Creative Commons Attribution (CC BY) license (<https://creativecommons.org/licenses/by/4.0/>).

## 1. Introduction

Surface plasmon resonance (SPR) are generated by the coherent oscillations of conduction electrons at a metal–dielectric interface film [1], leading to intriguing physical phenomena, such as extraordinary optical transmission (EOT) [2], responses to surrounding environment [3], light trapping [4], and hot spots [5]. These properties facilitate many applications, such as optical filters [6], sensors [7], antireflection layers [8], and imaging [9]. Great efforts are made to develop different nanostructures to achieve stronger resonance and expand the application prospects. Typical plasmonic models of planar metal films with a coupler (Kretschmann configuration) [10], nanoparticles [11], and nanohole arrays [12] have been fabricated and show impressive performance.

Recently, plasmonic films with various three-dimensional (3D) nanostructures have been prepared and show stronger resonance and higher index sensitivity [13–16]. Based on these results, we have proposed that 3D nanostructures, which can make enhanced electric field distributed in air, not in the substrate, represent a qualitative advancement of plasmonic sensors [17]. In particular, we introduced an anomalous phenomenon that light easily passes through an optically thick continuous film which was prepared with a periodic array of hollow nanocones [18]. Different from widely investigated solid nanocones, the plasmonic films with hollow nanocone arrays possess a resonance cavity with top tips and bottom nanoholes, leading to strong coupling between propagating surface plasmon polariton (SPP) along the film and localized SPR (LSPR) of the top tips. Besides the fundamental interest, novel SPR modes would emerge by changing the interface between the structure and dielectric, leading to distinctive spectra. To develop an analysis with these, however, one has to understand precisely the local field distribution and their influence on optical properties. This should then help to measure quantitatively environmental changes in and near the cavities.

In this paper, hollow nanocone arrays are fabricated by an efficient colloidal lithography method and further are inversed, making the tips contact the substrate and the film covering on top. The inverse hollow nanocone arrays are not simply reversed but lead to brand new resonance modes and great advances in sensing and fluorescence enhancement. Reflection spectra of both the obverse and inverse structured arrays are measured from two opposite vertical directions relative to the sample. SPP along the films and LSPR on the nanocones are strongly coupled. The resonance modes in different cases and the effect of structural parameters are investigated, showing the dominant role of the interface and its control over the spectra. Furthermore, the inverse hollow nanocone arrays show a relative sensitivity up to 70% per RIU to the changes of the surrounding environment, following a strict linear dependence. Surface enhanced fluorescence is tested and can be facilely realized by placing the fluorophore on the hollow nanocone array films. The hollow nanocone arrays are expected to develop the plasmonic sensors and serve as a versatile substrate for enhanced fluorescence imaging.

## 2. Materials and Methods

### 2.1. Materials

All the water used in this work is ultrapure deionized with 18.2 M $\Omega$ -cm. Polystyrene (PS) spheres with the diameter of 700 nm and photoresist (BP212-37 positive photoresist) were purchased from Wuhan Tech Co., Ltd. (Wuhan, China) and Kempur (Beijing, China) Microelectronics, Inc. (Hilliard, OH, USA), respectively. Silver (99.9%) powder (51022866) for thermal-deposition, Polyvinyl alcohol (PVA) (30153083), and Rhodamine B (RhB) (71036314) were purchased from Sinopharm Chemical Reagent Co. Ltd. (Shanghai, China) Dichloromethane (XW00750922), methanol (10014190), ethanol (XW00641751), and other reagents were purchased from Sinopharm Chemical Reagent Co. Ltd. and used, as received. Polyethylene terephthalate (PET) film (ES30-FM-000160) was purchased from Goodfellow Cambridge Ltd. (Huntingdon, UK). Albumin from bovine serum (A1933) and tetramethylrhodamine B isothiocyanate (TRITC) labeled phalloidin (P1951) were obtained from Sigma-Aldrich (St. Louis, MI, USA). Triton X-100 (AR-0341) and 4% polyoxymethylene (AR-0211) was purchased from Beijing DINGGUO Biotechnology.

### 2.2. Fabrication of Obverse and Inverse Hollow Nanocone Array Films

Obverse hollow nanocone arrays were fabricated based on the colloidal lithography technique [18]. For fabricating the inverse hollow nanocone arrays, the obverse Ag nanocone array with the photoresist remaining between the Ag film and the substrate was laid inversely onto another glass substrate in a small vessel. Ethanol was dripped slowly into the vessel to submerge the Ag nanocone arrays. The photoresin was dissolved by ethanol. The upper (original) glass substrate was lifted from the vessel, and ethanol was also sucked away, leaving the hollow nanocone array inversely supported on the bottom glass substrate. Finally, inverse hollow nanocone arrays were obtained by taking the sample from the vessel and blowing it dry carefully.

### 2.3. Preparation of the Fluorescent Film

The 2.5 g PVA was dissolved by deionized water and diluted to 5%. Then, 0.0121 g RhB was put in 50 mL the PVA solution to obtain a concentration of  $5 \times 10^{-4}$  mol/L. Then the solution was first spin-coated onto a glass substrate at a rotation frequency of 800 r/s for 18 s, and subsequently was spin-coated onto the same substrate under rotation with 2000 r/s for 60 s. The thickness of the fluorescent film was ~100 nm, which was measured by a step profiler.

### 2.4. Cell Seeding and Staining

Flat PET films were used as the substrates for cell adhesion. Mouse MC3T3-E1 osteoblasts were cultured for 3 days with a density of  $1.5 \times 10^5$  cells per mL in H-DMEM media in 5% CO<sub>2</sub> at 37 °C. The H-DMEM consisted of 10% fetal bovine serum (FBS) (Gibco)

and 1% antibiotics (25,000 IU mL<sup>-1</sup> penicillin and 25 mg mL<sup>-1</sup> streptomycin). After culturing for 3 days, the substrates with cells adhered were washed in PBS for three times to remove the physically absorbed organics and prepared for staining.

For straining, the cells were immersed in polyoxymethylene (4%) in PBS solution for 20 min and then permeabilized in Triton X-100 (0.1%) for 10 min. After that, the cells were immersed in bovine serum albumin (3%) solution (blocking agent) for 2 h at room temperature. The cells were then washed twice by PBS buffer. We drew the TRITC-phalloidin solution by a pipet and dripped a few drops of the TRITC-phalloidin solution onto the cells. The cells with TRITC-phalloidin solution were incubated for 1 h at room temperature and then washed for three times by PBS.

### 2.5. Finite-Difference Time-Domain (FDTD) Calculations

A commercial software package (FDTD Solutions, Lumerical Solutions Inc., Vancouver, BC, Canada) was used to calculate the spectra and electric field distribution. First, structure models were constructed, and their parameters were extracted from the real samples. A plane source with normal incidence and  $x$  polarization was applied. The boundary conditions along the  $x$  and  $y$  axis are Periodic. Perfect metal layer (PML) was used for the  $z$  axis. The monitor of Frequency-domain field profile was used to calculate the electric field distribution. The spectra were obtained from the monitor of frequency-domain field and power. The mesh refinement is conformal variant 2. The software of ParaView was used to process the data of the electric field distribution.

### 2.6. Characterization

Scanning electron microscopy (SEM) images were taken with a JEOL JSM 6700F field emission scanning electron microscope. The spectra were measured by a Maya 2000PRO optics spectrometer with a remote UV/vis light source (DT 1000 CE). An HPX-2000 Xe Lamp (35 W), a MonoScan2000 monochromator, and a Maya 2000PRO optics spectrometer were used to measure the fluorescence spectra. The configuration of the spectrum measurements is shown in Figure S1 in Supporting Information. These optics devices are from Ocean Optics. The fluorescent microscope images were taken by an optical fluorescence microscope (Olympus BX51).

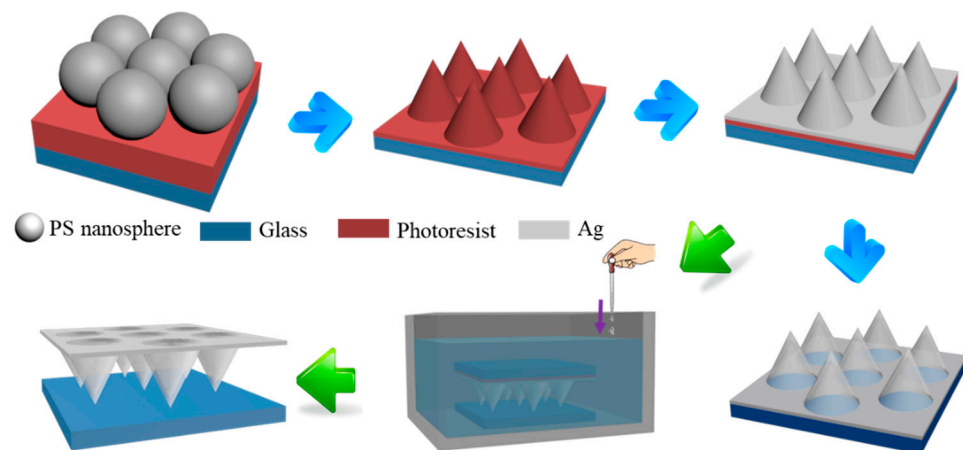
## 3. Results and Discussions

### 3.1. Fabrication Process and Characterization

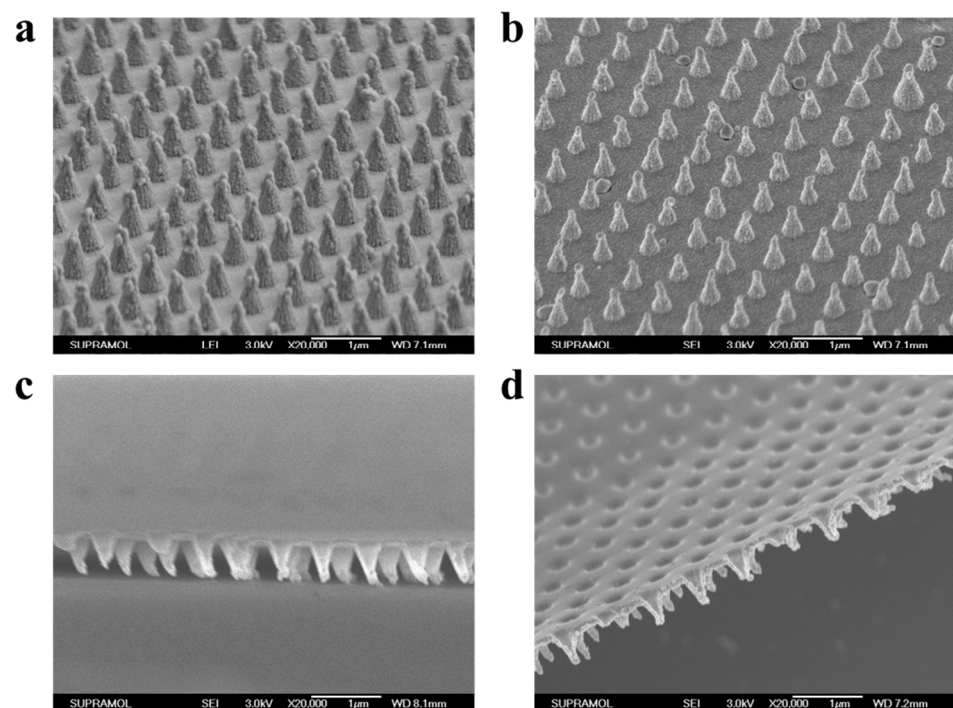
Figure 1 shows the fabrication process of the obverse and inverse hollow nanocone arrays. In brief, PS spheres were self-assembled by an interface method to form a highly ordered monolayer on a photoresin film. By using the PS spheres as the mask, reactive ion etching (RIE) was carried out to etch the photoresin film into a periodic cone array. The as-prepared sample was then deposited with Ag and washed in ethanol to remove the photoresin, creating an obverse hollow nanocone array. To prepare inverse hollow nanocone arrays, the substrate with the Ag cones and photoresin was flipped to make the tips of the cones contact another glass substrate. The photoresin was dissolved by ethanol in this reverse configuration. The hollow nanocone array films will detach the original (upper) substrate and fall onto the new (bottom) substrate, forming the inverse hollow nanocone arrays. The lattice constant (period), thickness, and height of the hollow nanocone arrays can be well controlled by the size of the PS spheres, deposition parameters, and etching process, respectively. The method can be implemented with a simple and inexpensive experimental setup. The nanostructures can be fabricated in a large area (>cm<sup>2</sup>) parallelly in a short time.

Figure 2a shows the SEM image of the obverse hollow nanocone array. Clearly, cones were formed in a periodic array. The height and diameter are ~500 nm and ~330 nm, respectively. The surface of the cones is rather rough with apparent trenches and nanoparticles. The trenches were formed in the RIE process. In the deposition process, spontaneous adatom diffusion, desorption, and reemission could induce adatom clustering,

re-evaporation, or capture at defect sites, leading to the nonhomogeneous distribution of Ag, i.e., forming the nanoparticles. The cones shrink with smaller height and smaller diameter by increasing the RIE duration. The obverse hollow array with the height of 300 nm and diameter of 200 nm is shown in Figure 2b. The cone shape is kept, while with a smaller size. Figure 2c,d shows the SEM images of the inverse hollow nanocone arrays corresponding to those in Figure 2a,b. The inverse hollow nanocone arrays show well-defined cones, which are the same as those of the obverse hollow nanocone arrays. The inverse hollow nanocone array films are supported only by the tips and remain well integrated.



**Figure 1.** Schematic of the fabrication process of the obverse and inverse hollow nanocone arrays.



**Figure 2.** SEM images with 45° tilting angle of the obverse hollow nanocone arrays with the height/diameter of (a) ~500/330 nm and (b) ~300/200 nm. Lateral SEM images of the inverse hollow nanocone arrays with the height/diameter of (c) ~500/330 nm and (d) ~300/200 nm.

### 3.2. Optical Properties and FDTD Calculations

Figure 3 shows the reflection spectra and simulations of the obverse and inverse hollow nanocone arrays with the height/diameter of ~500/330 nm. The morphology is a type of plasmonic grating, leading to strong coupling between SPP along the film and LSPR on the



nanocones. Different SPR modes are excited by changing the surrounding environment, leading to distinctive spectra. When illuminating on the back of the obverse hollow nanocone array, there appears a dip at about 950 nm, which is in qualitative agreement with the calculated spectrum (Figure 3a). Judged from the electric field simulated at the dip wavelength in Figure 3b, the enhanced electric field is mainly concentrated in the glass substrate. When illuminated on the inverse hollow nanocone array, a more prominent dip is observed at 767 nm (Figure 3c). The measured spectrum is consistent with the calculated spectrum. The differences between the spectra may be because the real samples are not as perfect as the calculated models, such as the rough surface, defects, and inhomogeneity of size. The calculated distribution of the electric field in Figure 3d shows that all the enhanced SP energy is redistributed in air, which makes it fully accessible to the species to be detected. This would greatly promote the sensitivity and linearity as demonstrated in the following discussion. In addition, the reflection spectra were also measured for other cases, where light illuminates the front of the hollow nanocone array. However, the spectra do not show well-defined peaks or dips, which thus can hardly be used in further applications (Figure S2).

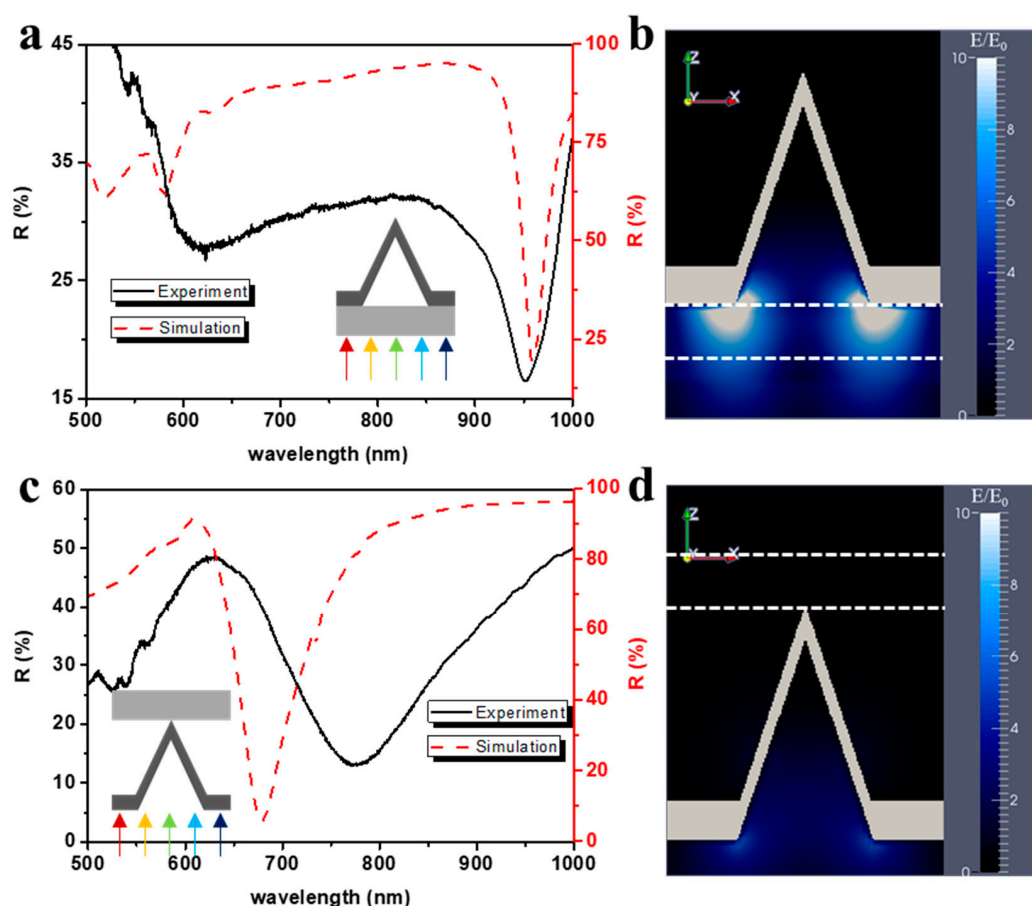


**Figure 3.** (a) Experimental (black solid curve) and calculated (red dotted curve) reflection spectra of the obverse hollow nanocone arrays. (b) Calculated distribution of the electric field at the dip wavelength of 950 nm. (c) Experimental (black solid curve) and calculated (red dotted curve) of the inverse hollow nanocone arrays. (d) Calculated distributions of the electric field at the dip wavelength of 767 nm. The insets in (a,b) indicate the cases of measurements. The colored arrows indicate the white light and the illuminating direction. The black and red lines in (a,c) correspond to the left black and right red Y-axis, respectively. The dotted lines in (b,d) indicate the outline of the glass substrates.

Moreover, the effect of the structural parameters on the optical performance was investigated, as shown in Figure 4. For the inverse hollow nanocone arrays, the dips shift to blue, and their depth become smaller as the height decreases, while the reflection

intensity becomes stronger (Figure 4a). This is due to the fact that the structure of the hollow nanocone array is getting closer to a planar film with decreasing height, leading to weaker resonance. In addition, the distance between the glass substrate and the upper film becomes smaller as the height decreases, which makes the resonance on the film become more affected by the glass substrate. Thus, an apparent blue shift is observed when the cones shrink. For the obverse hollow nanocone array in Figure 4b, the stronger reflection intensity and shrunk dips are also understood, as the structure of the hollow nanocone array becomes closer to that of a planar Ag film as the height decreases. However, as the glass always dominates the resonance, there is little shift in the dip wavelength. The results lead to the conclusion that the spectra are well and predictably controlled by the structural parameters. The inverse hollow nanocone arrays show the better identified dips and possess a redistribution of the electric field, promising high performance in sensing.

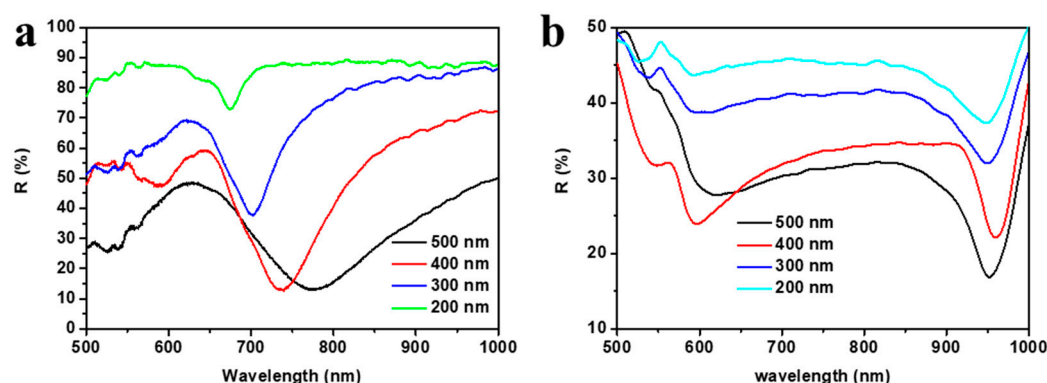


**Figure 4.** Reflection spectra of (a) inverse and (b) obverse hollow nanocone arrays with the height of 500 nm, 400 nm, 300 nm, and 200 nm.

### 3.3. Sensing Performance

The peaks or dips of plasmonic nanostructures could show responses to changes in the refractive index (RI) of the material around the nanostructure. Different materials have different RI, which can be identified by the peak/dip shift of the plasmonic nanostructures, forming the basis for plasmonic sensors. When evaluating a plasmonic sensor, the refractive index sensitivity (RIS) is mostly considered. The RIS of a wavelength interrogated sensor is defined in terms of the change in peak position ( $\Delta\lambda$ ) per 'refractive index ( $n$ ) unit' (RIU),  $RIS = \Delta\lambda / \Delta n$ . The response of the inverse hollow nanocone arrays to liquids with different RI was tested. The dips of the inverse hollow nanocone arrays with the height of 500 nm continuously shift to red with increasing RI (Figure 5a). Plots of the dip wavelength with RI of the inverse hollow nanocone arrays with different height are shown in Figure 5b. Linear fitting was applied to the plot, where the value of the slope is the value of the sensitivity. The dip wavelength shows strict linear dependence with RI with large coefficient of determination ( $R^2$ ). The sensitivity of the hollow nanocone arrays with the height of 500 nm, 400 nm, 300 nm, and 200 nm is 722 nm/RIU, 687 nm/RIU, 622 nm/RIU, and 580 nm/RIU, respectively. The hollow nanocone array with the height of 500 nm achieves the highest sensitivity of 722 nm/RIU, which is much higher than those of previous plasmonic sensors, including nanohole arrays (400 nm/RIU) [19], random nanoholes (71~270 nm/RIU) [20,21], and nanoparticles arrays (76~200 nm/RIU) [22,23]. Moreover, it is about 1.5-fold higher than the sensitivity of the transmission peak of the obverse hollow nanocone arrays [18]. In addition, as the height decreases, the linearity becomes worse (Figure 5b), and the sensitivity also decreases (Figure 5c).

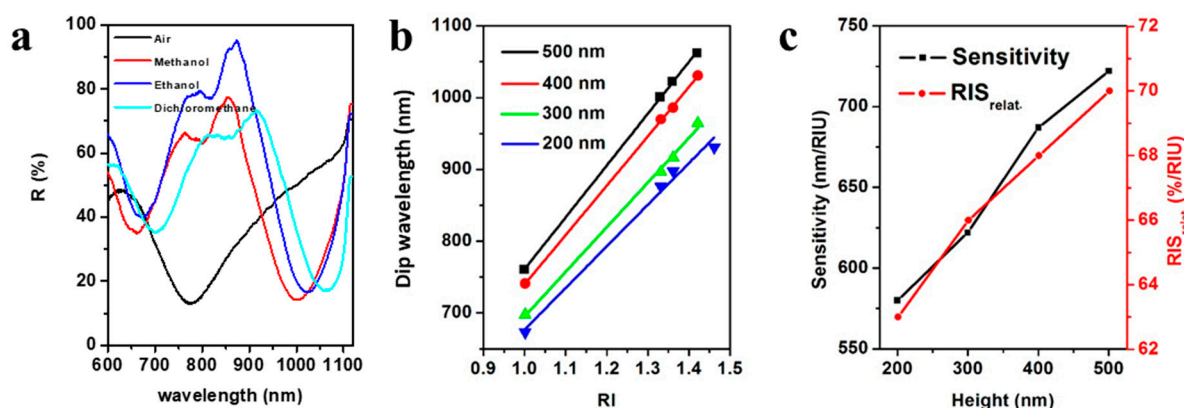


**Figure 5.** (a) Reflection spectra of the inverse hollow nanocone array with height of 500 nm measured by dripping a sequence of liquids with increasing RI: methanol (1.33), ethanol (1.36) and dichloromethane (1.42) on the sample. (b) Linear fits for the hollow nanocone arrays with height of 500 nm ( $R^2 = 0.99973$ ), 400 nm ( $R^2 = 0.99967$ ), 300 nm ( $R^2 = 0.99664$ ) and 200 nm ( $R^2 = 0.98559$ ). (c) Graph showing the sensitivity and related sensitivity as function of the height.

For plasmonic nanostructure arrays, RIS has a positive dependent relationship with period, and would increase as period becomes larger [24]. Additionally, it was reported that RIS became higher when the nanostructure has a larger feature size [25]. So, RIS may not be a good parameter to be used to compare the quality of plasmonic sensors with different periods or feature sizes. Rather, Shumaker-Parry and coworkers introduced the relative RIS as a universal factor to make such a comparison [25]:

$$\text{RIS}_{\text{relat.}} = \frac{1}{\omega_r} \times \frac{\Delta\omega(\text{eV})}{\Delta n} \times 100\%$$

$\omega_r$  is the initial resonance energy in units of eV.  $\Delta\omega/\Delta n$  is the bulk RIS with units of eV per RIU. The dip energy of each spectrum measured for different liquids was first determined and then plotted with RI. Linear fitting was applied to the plot, where the value of the slope is the value of  $\Delta\omega/\Delta n$ . The relative RIS of the hollow nanocone arrays with different height is shown in Figure 5c. Clearly, the relative RIS of the sample with the height of 500 nm is up to 70% per RIU and is the highest. This value is higher than that of crescents (38%) [25], hematite-gold core-shells or rices (40%) [26], nanoholes (61%) [27], and the obverse hollow nanocone arrays (64%) [18].

The enhanced performance of the robust linear response results from the great enhancement and redistribution of the electric field. The hollow nanocone arrays can be split into two parts of the bottom nanohole array and the upper tips. For the nanohole arrays, SPP and LSPR were excited along the film and at the holes [28], respectively, resulting in extraordinary optical transmission (EOT) [12]. The sharp nanocone tips are the pronounced places where the LSPR energy is focused, making the electric field intensity of nanocones much stronger than that of other nanostructures [29,30]. The hollow cone tip and nanohole could support partially localized SPRs (LSPRs), and as the propagating surface plasmon polariton (SPP) is excited along the film, the coupling of the LSPRs and SPP lead to redistribution and greater enhancement in electric field. For the inverse hollow nanocone array, the tip contacts the substrate, and the film suspends upon the substrate. The inverse hollow nanocone array is like a free-standing film without the effect of the substrate. The environment on the two sides of the surface is both air. The same environment matches the SP mode frequencies at both interfaces of the inverse hollow nanocone array, leading to the most efficient coupling. In addition, the enhanced electric field is not confined in the substrate, while distributed in air, where the enhanced SP energy is fully accessible to species to be detected. The stronger SP energy and more accessible distribution of SP energy make the inverse hollow nanocone array possess higher sensing performance. As the height decreases, the substrate contributes more to the resonance and would make

the SP energy less matched, resulting in weaker enhancement of the electric field. The enhanced electric field is less distributed in air, making part of the enhanced SP energy not accessible to the detected species. The weaker SP energy and greater distribution of the SP energy in substrate lead to the deviation from linearity and reduced sensitivity with decreasing height.

### 3.4. Surface Enhanced Fluorescence

Based on the unique structure and resonance modes, the hollow nanocone arrays can be used as versatile substrates for fluorescence enhancement. This is easily realized just by placing the fluorophore on the hollow nanocone array film. Different cases as shown in Figure 6a were measured to demonstrate the property of surface enhanced fluorescence. First, polyvinyl alcohol (PVA) doped with rhodamine B (RhB) was spin-coated on a glass substrate. Light is impinging from the upper side in all six cases. Figure 6b shows the fluorescence spectra. Comparing case 1 with 2, the intensity of the black line (case 1) is slightly larger than that of the red line (case 2) due to the optical loss through the glass in case 2. When the substrate coated with RhB/PVA was placed on the inverse hollow nanocone array, the intensity of case 3 was much enhanced compared with that of case 1. The intensity was also greatly enhanced from case 2 to case 4. This type of comparison between the fluorescence film with and without nanostructures has always been shown in previous work [31–36]. However, we consider the comparison as not being justified because the Ag film possesses stronger reflection than the glass substrate, and this enhances the excitation light and the reflection of the fluorescence. In other words, the fluorescence enhancement derives much from the inherent quality of strong reflection of the Ag film, not only the plasmonic effect. In previous reports, the quantity of fluorophore in the compared systems could hardly be the same, also resulting in a difference of fluorescence intensity. As a result, the surface enhanced fluorescence is an overall effect with different contributions. In this work, based on the unique form of fluorescence enhancement, we remove other factors and obtain only the plasmonic effect via controlling whether the fluorescence dye could directly contact the Ag film or not. When RhB/PVA contacts the metal (case 4), the enhanced SP energy increases the excitation of the RhB, so that the intensity is stronger than that in the case when the SP energy cannot affect the fluorophore (case 3). Considering the thick interval in case 3, the SP energy does not affect the fluorescence intensity, as the range of the plasmonic effect is rather limited [34,37,38]. The enhancement from case 3 to 4 only derives from the plasmonic effect, which clearly shows the real surface enhanced fluorescence based on plasmonic materials. The representation of the real plasmonic effect on surface enhanced fluorescence is very useful for clarifying the mechanism and precise instrumentation.

Furthermore, the obverse hollow nanocone arrays were also measured to assess the fluorescence enhancement (case 5 and 6). The absolute intensity is lower than that of the inverse sample, and this is due to the weaker reflection of the obverse hollow nanocone arrays at the excitation and emission wavelengths (Figures 3a and S2). In contrast, the difference of the obverse sample is much larger than that of the inverse sample, indicating a stronger real surface enhanced fluorescence. To demonstrate the phenomenon, electric field distributions were simulated as shown in Figure 6c,d. When the bottom film contacts the RhB/PVA in Figure 6c, the electric field is weak and concentrated on the interface between the Ag film and RhB. When the tip contacts the RhB/PVA, the electric field is concentrated on the external surface of the cone and extends outside into the RhB/PVA layer (Figure 6d). The intensity is also much larger than in Figure 6c. The strong intensity and the extension of the SP energy in the fluorophore lead to a stronger plasmonic effect on the fluorescence. In addition, the dye fluorescence is quenched when it has a distance to the metal less than 5 nm [37]. For the obverse hollow nanocone array, only the tips contact the fluorescent material, resulting in a point contact. The contacting area is much smaller than the inverse sample, which greatly reduces the quench. This also contributes to the higher fluorescence enhancement for the obverse hollow nanocone arrays.



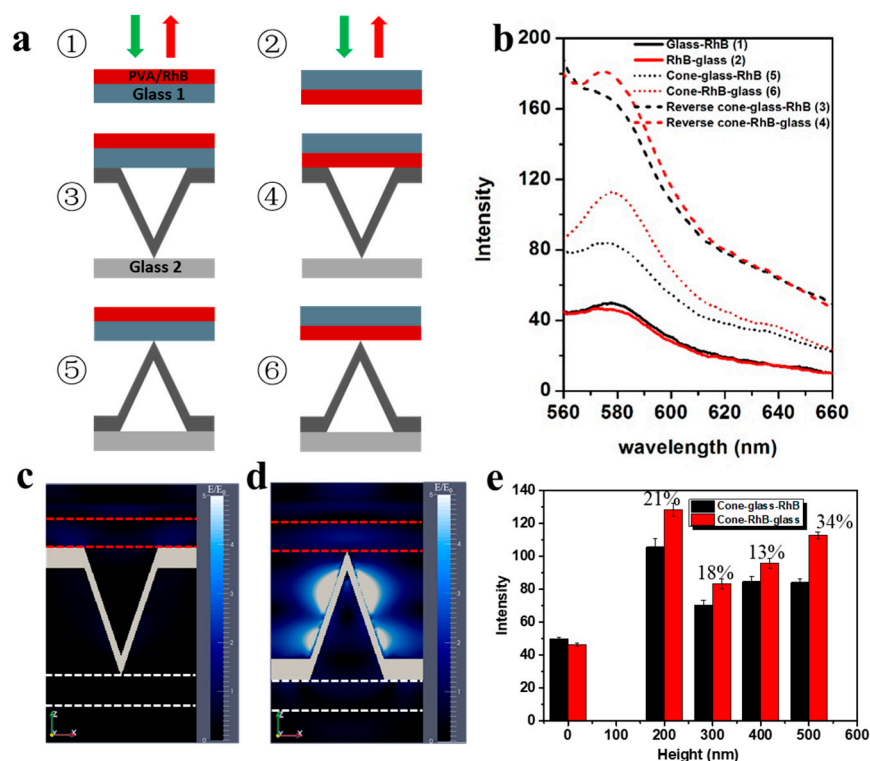


**Figure 6.** (a) Schematics of the measuring cases. The green arrow indicates the incident light, and the red arrow indicates the fluorescence collected by the detector, applying to all six cases. The glass 1 indicated by blue is connected with the PVA/RhB layer. The glass 2 indicated by grey supports the hollow nanocone array. (b) Fluorescence spectrum of the cases in (a). (c) Simulated distribution of the electric field in the case 4 at 525 nm. (d) Simulated distribution of electric field in the case 6 at 525 nm. The white and red dotted lines indicate the contours of the glass substrate and RhB/PVA film, respectively. (e) A histogram showing the fluorescence intensity of cases 1 and 2 and of the samples with height of 200 nm, 300 nm, 400 nm and 500 nm in case 6.

Figure 6e shows the fluorescence enhancement of the samples with different heights. The intensity of the hollow nanocone arrays is larger than the intensity of the glass substrates (cases 1 and 2). The intensity of the sample with a height of 200 nm is the largest, and the intensity is enhanced by 34%, 13%, 18% and 21% for the samples with the heights of 500 nm, 400 nm, 300 nm, and 200 nm, respectively. The fluorescence intensity and enhancement are determined by the light reflection from the Ag film and plasmonic enhanced electric field. The light reflection from the Ag film decreases when the height of the nanocone becomes larger, as shown in Figure 4b. For the sample with the height of 200 nm, the light reflection is the strongest, thus leading to the largest fluorescence intensity. The plasmonic enhanced electric field increases with the height [18]. When the height is 500 nm, the enhanced electric field is the strongest, and thus the fluorescence enhancement is the largest. For the samples with the height of 300 and 400 nm, the light reflection and enhanced electric field become weaker, leading to the lower intensity and smaller difference. The enhancement can be well made use of in fluorescence imaging.

Cells stained with TRITC-phalloidin, supported on PET substrates, were investigated for demonstration of the enhanced fluorescence imaging. Figure 7a shows the fluorescence image of the sample without the structured films for an exposure duration of 1000 ms. Figure 7b,c shows the fluorescence microscopy images in different cases, where the PET substrate contacts the tip, such that the cell cannot contact the metal structure (case 5) and where the cells are supported by the tips (case 6), respectively. For the same exposure duration (300 ms), the cells cannot be recognized without the support of the hollow nanocone array film. Even for much longer exposure duration, the brightness of the cells is weaker than that on the metal film, comparing Figure 7a with Figure 7b,c. This demonstrates the

great enhancement derived from the hollow nanocone array films. Furthermore, enhanced fluorescence is observed through the comparison of the cells marked by the numbers in Figure 7b,c. The imaging of the cells is more distinct when the hollow nanocone arrays directly contact the cells (Figure 7c, case 6), contributing a plasmonic effect to the fluorescence. This is helpful for biological detection and fluorescence imaging. Based on the facile operations of fluorescence enhancement and transferability, the hollow nanocone arrays can be used as versatile substrates to enhance the fluorescence image.

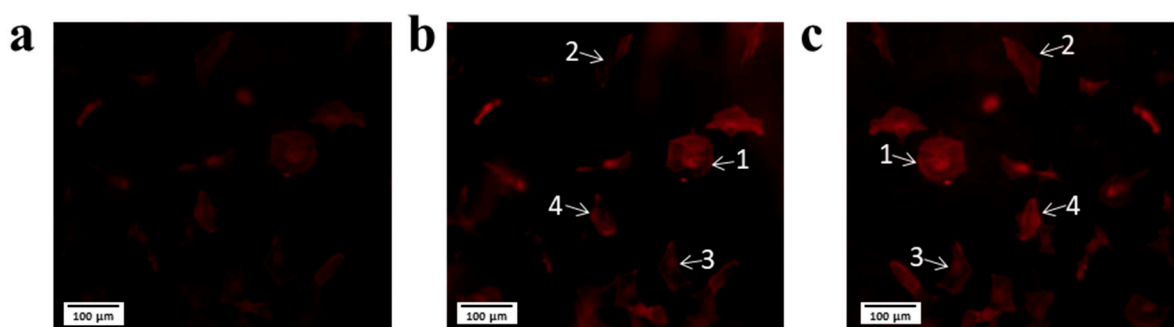


**Figure 7.** Fluorescence microscopy images in the cases (a) when the cell/PET is without the structured films with exposure duration 1000 ms (b) when the PET substrate contacts the tips (case 5) and (c) when the cells were supported by the tips (case 6). The images (b,c) were exposed for 300 ms. The numbers in (b,c) point to the nearby cells to clearly show the comparison.

#### 4. Conclusions

In summary, both obverse and inverse hollow nanocone arrays are fabricated via an efficient colloidal lithography method and a facile transfer process. The topologically continuous films show strong coupling between SPP and LSPR, and different resonance modes as the interface and the illuminated direction change, resulting in pronounced features of the reflection spectra. Calculations show good agreement with the measured spectra. Well-defined dips emerge in the spectra of inverse hollow nanocone arrays and show high refractive index sensitivity with a strict linear relationship. Fluorescence is easily enhanced by placing the fluorescent materials on the tips of the obverse hollow nanocone arrays. The strong SP energy increases the excitation of the fluorescence, and the small contact area between metal and fluorescent film can greatly reduce the fluorescence quenching. In addition, the effect of different configuration (obverse and inverse) of the same nanostructure on the plasmonic properties is revealed, which would benefit the understanding of the working principle of SPR. The study of the hollow nanocone arrays with different configurations not only deepens the cognition of the dependence of SPR on structure and environment, but also exhibits great potential to develop plasmonic sensors and fluorescence imaging.

**Supplementary Materials:** The following supporting information can be downloaded at: <https://www.mdpi.com/article/10.3390/chemosensors10100431/s1>, Figure S1: Measurement configuration. Figure S2: Reflection spectra.

**Author Contributions:** Conceptualization, J.C. and B.A.; methodology, P.C.; software, X.C. and M.C.; validation, J.C. and B.A.; formal analysis, P.C.; investigation, P.C. and B.A.; resources, J.C.; data curation, P.C.; writing—original draft preparation, P.C., J.C. and B.A.; writing—review and editing, C.Z. and B.A.; visualization, P.C.; supervision, J.C. and B.A.; project administration, B.A.; funding acquisition, B.A. All authors have read and agreed to the published version of the manuscript.

**Funding:** This research was funded by the Open Project of State Key Laboratory for Supramolecular Structure and Materials (SKLSSM 202201).

**Institutional Review Board Statement:** Not applicable.

**Informed Consent Statement:** Not applicable.

**Data Availability Statement:** Not applicable.

**Conflicts of Interest:** The authors declare no conflict of interest.

## References

- Atwater, H.A. The promise of plasmonics. *Sci. Am.* **2007**, *296*, 56–63. [\[CrossRef\]](#) [\[PubMed\]](#)
- Ebbesen, T.W.; Lezec, H.J.; Ghaemi, H.F.; Thio, T.; Wolff, P.A. Extraordinary optical transmission through sub-wavelength hole arrays. *Nature* **1998**, *391*, 667–669. [\[CrossRef\]](#)
- Stewart, M.E.; Anderton, C.R.; Thompson, L.B.; Maria, J.; Gray, S.K.; Rogers, J.A.; Nuzzo, R.G. Nanostructured Plasmonic Sensors. *Chem. Rev.* **2008**, *108*, 494–521. [\[CrossRef\]](#) [\[PubMed\]](#)
- Farid, S.; Dixon, K.; Shayegannia, M.; Ko, R.H.H.; Safari, M.; Loh, J.Y.Y.; Kherani, N.P. Rainbows at the End of Sub-wavelength Discontinuities: Plasmonic Light Trapping for Sensing Applications. *Adv. Opt. Mater.* **2021**, *9*, 2100695. [\[CrossRef\]](#)
- Zhang, W.; Zheng, T.; Ai, B.; Gu, P.; Guan, Y.; Wang, Y.; Zhao, Z.; Zhang, G. Multiple plasmonic hot spots platform: Nanogap coupled gold nanoparticles. *Appl. Surf. Sci.* **2022**, *593*, 153388. [\[CrossRef\]](#)
- Inoue, D.; Miura, A.; Nomura, T.; Fujikawa, H.; Sato, K.; Ikeda, N.; Tsuya, D.; Sugimoto, Y.; Koide, Y. Polarization independent visible color filter comprising an aluminum film with surface-plasmon enhanced transmission through a subwave-length array of holes. *Appl. Phys. Lett.* **2011**, *98*, 093113. [\[CrossRef\]](#)
- Lim, K.; Jo, Y.M.; Yoon, J.W.; Kim, J.S.; Lee, D.J.; Moon, Y.K.; Yoon, J.W.; Kim, J.H.; Choi, H.J.; Lee, J.H. A Transparent Nanopatterned Chemiresistor: Visible-Light Plasmonic Sensor for Trace-Level NO<sub>2</sub> Detection at Room Temperature. *Small* **2021**, *17*, 2100438. [\[CrossRef\]](#)
- Park, J.; Kang, I.-S.; Sim, G.; Kim, T.H.; Lee, J.-K. Broadband responsivity enhancement of Si photodiodes by a plasmonic antireflection bilayer. *Opt. Express* **2021**, *29*, 26634–26644. [\[CrossRef\]](#)
- Rezaei, S.D.; Dong, Z.; Chan, J.Y.E.; Trisno, J.; Ng, R.J.H.; Ruan, Q.; Qiu, C.-W.; Mortensen, N.A.; Yang, J.K. Nanophotonic Structural Colors. *ACS Photonics* **2021**, *8*, 18–33. [\[CrossRef\]](#)
- Kretschm, E.; Raether, H. Radiative Decay of Non Radiative Surface Plasmons Excited by Light. *Z. Fur Nat. Part A-Astrophys. Phys. Phys. Chem. A* **1968**, *23*, 2135–2136.
- Lu, J.; Xue, Y.; Bernardino, K.; Zhang, N.-N.; Gomes, W.R.; Ramesar, N.S.; Liu, S.; Hu, Z.; Sun, T.; de Moura, A.F.; et al. Enhanced optical asymmetry in supramolecular chiroplasmonic assemblies with long-range order. *Science* **2021**, *371*, 1368–1374. [\[CrossRef\]](#) [\[PubMed\]](#)
- Genet, C.; Ebbesen, T.W. Light in tiny holes. *Nature* **2007**, *445*, 39–46. [\[CrossRef\]](#) [\[PubMed\]](#)
- Ai, B.; Yu, Y.; Moehwald, H.; Zhang, G. Novel 3D Au nanohole arrays with outstanding optical properties. *Nanotechnology* **2012**, *24*, 035303. [\[CrossRef\]](#) [\[PubMed\]](#)
- Ai, B.; Yu, Y.; Moehwald, H.; Zhang, G. Responsive Monochromatic Color Display Based on Nanovolcano Arrays. *Adv. Opt. Mater.* **2013**, *1*, 724–731. [\[CrossRef\]](#)
- Ai, B.; Wang, L.M.; Moehwald, H.; Yu, Y.; Zhang, G. Asymmetric half-cone/nanohole array films with structural and directional reshaping of extraordinary optical transmission. *Nanoscale* **2014**, *6*, 8997–9005. [\[CrossRef\]](#) [\[PubMed\]](#)
- Ai, B.; Wang, L.; Möhwal, H.; Yu, Y.; Zhang, G. Confined surface plasmon sensors based on strongly coupled disk-in-volcano arrays. *Nanoscale* **2014**, *7*, 2317–2324. [\[CrossRef\]](#)
- Ai, B.; Yu, Y.; Möhwal, H.; Zhang, G.; Yang, B. Plasmonic films based on colloidal lithography. *Adv. Colloid Interface Sci.* **2014**, *206*, 5–16. [\[CrossRef\]](#) [\[PubMed\]](#)
- Ai, B.; Yu, Y.; Möhwal, H.; Wang, L.; Zhang, G. Resonant Optical Transmission through Topologically Continuous Films. *ACS Nano* **2014**, *8*, 1566–1575. [\[CrossRef\]](#)
- Brolo, A.G.; Kwok, S.C.; Moffitt, M.G.; Gordon, R.; Riordon, J.; Kavanagh, K.L. Enhanced fluorescence from arrays of nanoholes in a gold film. *J. Am. Chem. Soc.* **2005**, *127*, 14936–14941. [\[CrossRef\]](#)
- Dahlin, A.; Zäch, M.; Rindzevicius, T.; Käll, M.; Sutherland, A.D.S.; Höök, F. Localized Surface Plasmon Resonance Sensing of Lipid-Membrane-Mediated Biorecognition Events. *J. Am. Chem. Soc.* **2005**, *127*, 5043–5048. [\[CrossRef\]](#)
- Rindzevicius, T.; Alaverdyan, Y.; Dahlin, A.; Höök, F.; Sutherland, D.S.; Käll, M. Plasmonic Sensing Characteristics of Single Nanometric Holes. *Nano Lett.* **2005**, *5*, 2335–2339. [\[CrossRef\]](#) [\[PubMed\]](#)
- Nath, N.; Chilkoti, A. Label-free biosensing by surface plasmon resonance of nanoparticles on glass: Optimization of nano-particle size. *Anal. Chem.* **2004**, *76*, 5370–5378. [\[CrossRef\]](#) [\[PubMed\]](#)
- Hartlen, K.D.; Athanasopoulos, A.A.P.T.; Kitaev, V. Facile Preparation of Highly Monodisperse Small Silica Spheres (15 to >200 nm) Suitable for Colloidal Templating and Formation of Ordered Arrays. *Langmuir* **2008**, *24*, 1714–1720. [\[CrossRef\]](#) [\[PubMed\]](#)
- Ai, B.; Basnet, P.; Larson, S.; Ingram, W.; Zhao, Y.P. Plasmonic sensor with high figure of merit based on differential polarization spectra of elliptical nanohole array. *Nanoscale* **2017**, *9*, 14710–14721. [\[CrossRef\]](#)
- Bukasov, R.; Shumaker-Parry, J.S. Highly Tunable Infrared Extinction Properties of Gold Nanocrescents. *Nano Lett.* **2007**, *7*, 1113–1118. [\[CrossRef\]](#)
- Wang, H.; Brandl, D.W.; Le, F.; Nordlander, P.; Halas, N. Nanorice: A Hybrid Plasmonic Nanostructure. *Nano Lett.* **2006**, *6*, 827–832. [\[CrossRef\]](#)

27. Li, Y.; Pan, J.; Zhan, P.; Zhu, S.; Ming, N.; Wang, Z.; Han, W.; Jiang, X.; Zi, J. Surface plasmon coupling enhanced dielectric environment sensitivity in a quasi-three-dimensional metallic nanohole array. *Opt. Express* **2010**, *18*, 3546–3555. [[CrossRef](#)]
28. Gao, H.; Henzie, J.; Odom, T. Direct Evidence for Surface Plasmon-Mediated Enhanced Light Transmission through Metallic Nanohole Arrays. *Nano Lett.* **2006**, *6*, 2104–2108. [[CrossRef](#)]
29. Martín-Cano, D.; Martín-Moreno, L.; García-Vidal, F.J.; Moreno, E. Resonance Energy Transfer and Superradiance Mediated by Plasmonic Nanowaveguides. *Nano Lett.* **2010**, *10*, 3129–3134. [[CrossRef](#)]
30. Chen, Y.; Cruz-Chú, E.R.; Woodard, J.C.; Gartia, M.R.; Schulten, K.; Liu, L. Electrically Induced Conformational Change of Peptides on Metallic Nanosurfaces. *ACS Nano* **2012**, *6*, 8847–8856. [[CrossRef](#)]
31. Hao, Q.; Du, D.; Wang, C.; Li, W.; Huang, H.; Li, J.; Qiu, T.; Chu, P.K. Plasmon-induced broadband fluorescence enhancement on Al-Ag bimetallic substrates. *Sci. Rep.* **2014**, *4*, 6014. [[CrossRef](#)] [[PubMed](#)]
32. Ray, K.; Chowdhury, M.H.; Lakowicz, J.R. Aluminum Nanostructured Films as Substrates for Enhanced Fluorescence in the Ultraviolet-Blue Spectral Region. *Anal. Chem.* **2007**, *79*, 6480–6487. [[CrossRef](#)] [[PubMed](#)]
33. Qiu, T.; Jiang, J.; Zhang, W.; Lang, X.; Yu, X.; Chu, P.K. High-Sensitivity and Stable Cellular Fluorescence Imaging by Patterned Silver Nanocap Arrays. *ACS Appl. Mater. Interfaces* **2010**, *2*, 2465–2470. [[CrossRef](#)] [[PubMed](#)]
34. Akbay, N.; Lakowicz, J.R.; Ray, K. Distance-Dependent Metal-Enhanced Intrinsic Fluorescence of Proteins Using Polyelectrolyte Layer-by-Layer Assembly and Aluminum Nanoparticles. *J. Phys. Chem. C* **2012**, *116*, 10766–10773. [[CrossRef](#)] [[PubMed](#)]
35. Mackowski, S.; Wormke, S.; Maier, A.J.; Brotsudarmo, T.H.P.; Harutyunyan, H.; Hartschuh, A.; Govorov, A.O.; Scheer, H.; Brauchle, C. Metal-enhanced fluorescence of chlorophylls in single light-harvesting complexes. *Nano Lett.* **2008**, *8*, 558–564. [[CrossRef](#)]
36. Song, J.-H.; Atay, T.; Shi, S.; Urabe, H.; Nurmikko, A.V. Large Enhancement of Fluorescence Efficiency from CdSe/ZnS Quantum Dots Induced by Resonant Coupling to Spatially Controlled Surface Plasmons. *Nano Lett.* **2005**, *5*, 1557–1561. [[CrossRef](#)]
37. Lakowicz, J.R.; Shen, Y.B.; D’Auria, S.; Malicka, J.; Fang, J.Y.; Gryczynski, Z.; Gryczynski, I. Radiative decay engineering 2. Effects of silver island films on fluorescence intensity, lifetimes, and resonance energy transfer. *Anal. Biochem.* **2002**, *301*, 261–277. [[CrossRef](#)]
38. Zin, M.T.; Leong, K.; Wong, N.-Y.; Ma, H.; Sarikaya, M.; Jen, A.K.-Y. Surface-plasmon-enhanced fluorescence from periodic quantum dot arrays through distance control using biomolecular linkers. *Nanotechnology* **2008**, *20*, 015305. [[CrossRef](#)]